[Journal of Geophysical Research: Solid Earth]

Supporting Information for

[Seismic imaging beneath Cascadia shows shallow mantle flow patterns guide lower mantle upwellings]

[Yuhang Dai[1], Catherine A. Rycherrt[1,2], Nicholas Harmon[1,2]]

[[1]Ocean and Earth Science, National Oceanography Centre Southampton, University of Southampton, Southampton, UK

[2]Geology & Geophysics Department, Woods Hole Oceanographic Institution (WHOI), Woods Hole, MA, USA]

Contents of this file

Introduction

[We show examples of RFs from on- and offshore data (Figure S1). We compare the on- and offshore datasets and melded them together (Text S1, Figure S2). We use different methods to testify the supra-410 phases (Text S2, Figure S3). We show hit counts maps (Figure S4) and error maps (Figure S5). Several seismic tomography results (Figure S6) suggest upwellings from the lower mantle beneath the study area. We show vertical cross-sections from different migration models (Figure S7).]

Text S1.

Variation in the character of the receiver functions between ocean and land stations is expected at shallow, crustal depths (Figure 4) given the very different crustal structures of the two. To demonstrate an example of the expected differences we constructed a synthetic receiver function from an oceanic model and one from a continental model (Figure S2 a). For the oceanic model, we assumed a 1 km sediment layer above a thin (6 km) oceanic crystalline crust under 3 km of water, and an underlying model taken from PREM (Dziewonski & Anderson, 1981). For the land model, we assumed PREM. We applied the same corrections to the synthetics that we apply to the data.

We find substantial differences at shallow depths between the ocean and land receiver function examples (Figure S1, S2). In particular, the most prominent phase in the continental receiver function is the red (positive) phase associated with the continental Moho near 20 km depth. Whereas, there is a large blue (negative) phase at nearby depths beneath the oceans, which is caused by interference between P-to-S conversions from the sediment and crustal layers and associated reverberations (Rychert et al., 2013). These differences are similar to those observed in the data (Figure 4). Although we provide a single example for demonstration, the exact details of these differences are expected to be variable owing to factors such as differences in shallow structure (e.g., depth variations of the sediment, Moho, and lithosphere-asthenosphere boundary (Rychert et al., 2018) and interference of reverberated phases. Given that reverberated phases are not properly accounted for in our migration approach, matching these characteristics is beyond the scope of this work, we are not performing waveform modeling, and we do not have any strong interpretation of phases shallower than 250 km depth.

The synthetic test demonstrates the robustness of the transition zone discontinuities. The depths of the transition zone discontinuities remain the same regardless of this shallow variability (Figure S2 a). In addition, supra-410 phases do not artificially appear in the ocean synthetic receiver functions. Also, reverberated phases from shallow discontinuities have completely died off by transition zone depths (Agius et

al., 2021). Some small phases just after the 410 and 660 discontinuities appear in the ocean synthetic receiver functions, but not the land receiver functions. We have seen similar phenomena in some of our previous modeling work that includes sediment (Rychert et al., 2013). However, we do not model these phases given that we are not interpreting those depths, and the phases don't impact the 410 or the 660 depths. We also note that although the ocean and land data have different corrections applied to them, given the theoretical difference in the positions of the seismometers beneath air vs. water and the physical differences in the underlying Earth properties. The corrections are an effective way of merging the two datasets.

We also compare receiver functions made by land vs. ocean data in a single bin (Figure S2 b). We find different characters between ocean vs. land data at shallow depths (< 30 km), similar to those found in the synthetic data. Similarly, variable reverberation effects contaminate the shallow 200 – 300 km. It is not our intention to model this exactly given the many potential complications. However, regardless of the differences in the shallow structure and corrections applied to account for this structure, the depths of the discontinuities are the same for the synthetic test and within our error bars for the data. This indicates that our theoretical corrections and variations in reverberations are not affecting our transition zone results.

Text S2.

We applied an iterative time-domain deconvolution (Ligorria & Ammon, 1999) to test the robustness of the supra-410 phases Time-domain deconvolution does not suffer from sidelobes, and therefore is an effective means of testing whether the supra-410 phases are sidelobe artifacts or actual conversions from the top of a supra-410 melt layer. We examined the data with theoretical piercing points in the two bins at 410 km depth with the strongest supra-410 phases (Figure 4 a, c, Figure 5 a). We filtered the waveforms between 0.05 and 0.2 Hz and used a Gaussian width factor of 3.5 for deconvolution. The stability of the time-domain deconvolution is different from the frequency-domain deconvolution. Therefore, we needed to remove 7 and 16 time-domain RFs without clear Moho phases or just pure spikes from the two bins,

respectively. We then migrated the 22 and 39 remaining waveforms to depth using sediment and crustal corrections and the IASP91 model, as done for the frequency domain RFs. We then stacked the RFs to construct the RFs for waveforms corresponding to the two bins characterized by large supra-410 phases (Figure S3 c, d). We stacked the waveforms in the bins in the original model from the multi-taper deconvolution for comparison (Figure S3 a, b). We scaled the time-domain RFs to have the same amplitudes for P410s phases as frequency-domain RFs.

The resulting stacked receiver functions are more complex than the 3-D model in that there are also other phases besides the 410, 660, and supra-410 phases. In addition, there are some differences between the methods. This is expected for two reasons: 1) These stacks were made with receiver functions that contribute to the supra-410 stacks in the 3-D model, but these RFs also sample a variety of different structures laterally at other depths. 2) The methods have different stabilities, which meant fewer waveforms were useable in the time domain stacks. Overall, the weighting and 3-D stacking that contribute to the stability and consistency of the 3-D model cannot be achieved using this small number of waveforms sampling different geographical areas at depths above and below the supra-410 phase. Therefore, we have no interpretation of phases at depths other than the 365 - 375 km depth range in these stacks. However, the test demonstrates that the supra-410 phase persists regardless of method, and in particular the phase persists in the time-domain method stacks, which are not susceptible to sidelobe artifacts.

We also note that the supra-410 phases are not artifacts of sediment deposited beneath the ocean near western North America. This is because the data in the supra-410 phase bins does not come from stations directly above, i.e., near the continental margin. Instead, the data in the supra-410 bins is primarily recorded at land stations further to the east.

In the end, we discuss the supra-410 phases given that their locations occur where we interpret upwelling based on the 410 topography, although these phases are not required for our interpretation of material transfer through the MTZ.

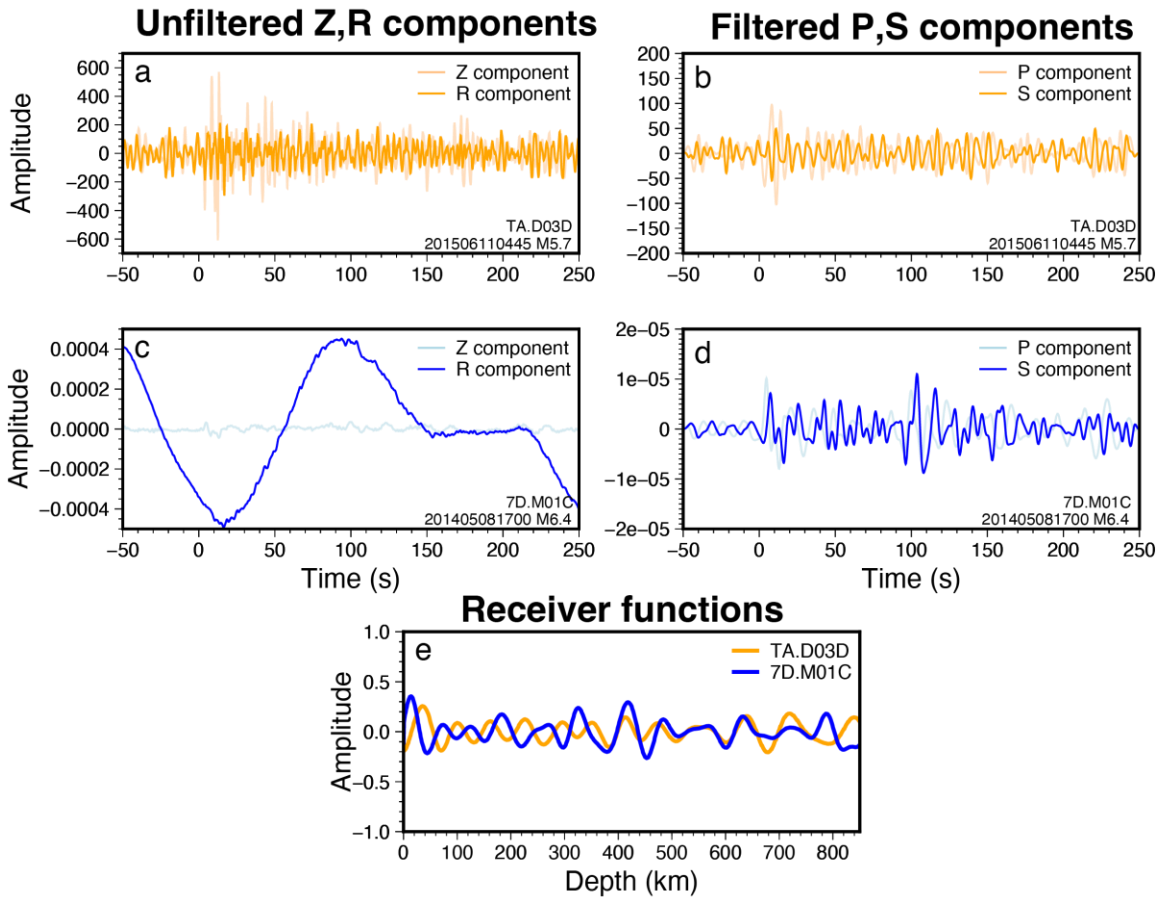

Figure S1. Examples of RFs from on- and off-shore data. a. unfiltered Z and R components of a M5.7 earthquake recorded by the onshore station D03D. b. filtered P and S components using a bandpass of 0.05 – 0.2 Hz correspond to a. c. unfiltered Z and R components of a M6.4 earthquake recorded by the offshore station M01C. d. filtered P and S components using a bandpass of 0.05 – 0.2 Hz correspond to c. e. Receiver functions correspond to b and d. The piercing points of these two receiver functions are both within the bin centered at 47.5° N, 126° W showed in Figure 5 a.

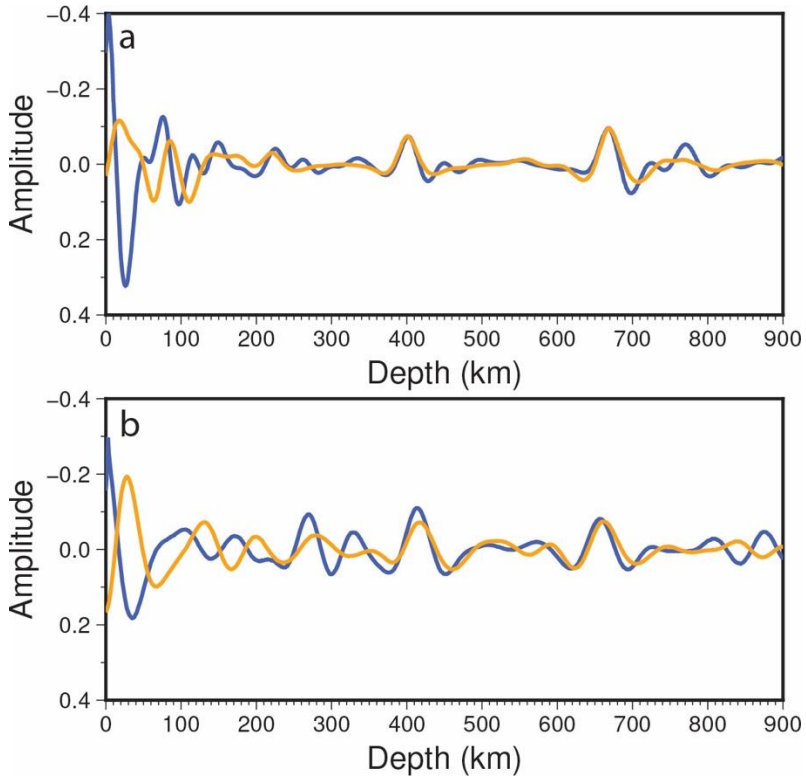

Figure S2. Onshore and offshore RFs comparations. a. Synthetic RFs. Orange line: RF from a synthetic land model using the parameters of crust and mantle from the reference earth model PREM (without a water layer), which has a crustal thickness of 21.4 km (Dziewonski & Anderson, 1981). Blue line: RF from a synthetic ocean model. The crust is set to be 6 km thick with Vp: 5.9 km/s and Vs: 3.4 km/s. The mantle is taken from the land model while adding a sediment layer with thickness: 1 km, Vp: 1.65 km/s, Vs: 1 km/s, Qκ: 163.35, Qμ: 80, and a water layer with thickness: 3 km, Vp: 1.45 km/s, Vs: 0 km/s, Qκ: 57823, Qμ: 0. b. Real RFs. Orange line: average RF from offshore data with piercing points at 410 km and 660 km within the bin shown in Figure 2 c, d. Blue line: average RF from OBS data with piercing points at 410 km and 660 km within the bin shown in Figure 2 c, d.

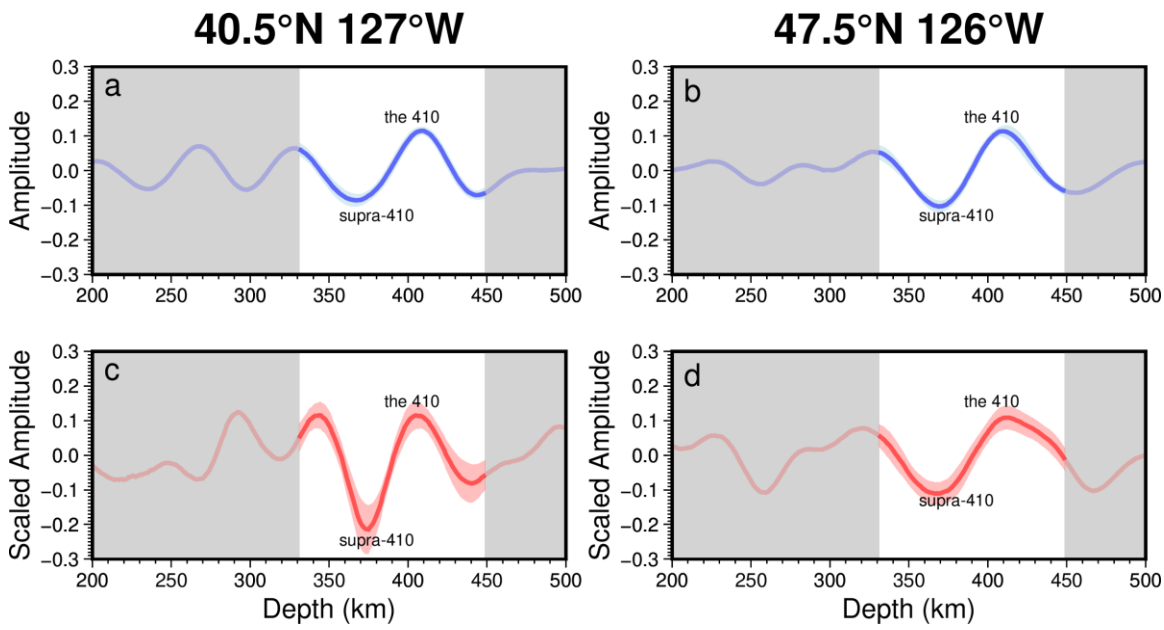

Figure S3. Stacked RFs using different deconvolution methods. a. Stacked RFs in the bin centered at 40.5°N, 127°W (Figure 5 a). The blue line shows the stacked result of RFs calculated using the multitaper frequency domain deconvolution technique (Helffrich, 2006), and light blue shows the standard deviation. Shaded areas show depths that are not interpretable, as they sample different Earth structures. b. same as a but for the bin centered at 47.5° N, 126° W. c. Red line shows the stacked RFs that pierce a bin centered at 40.5° N, 127° W at 410 km depth using iterative deconvolution in the time domain (Ligorria & Ammon, 1999), with the pink region showing error bars. d. Same as c but for the RFs that pierce a bin centered at 47.5° N, 126° W at 410 km depth.

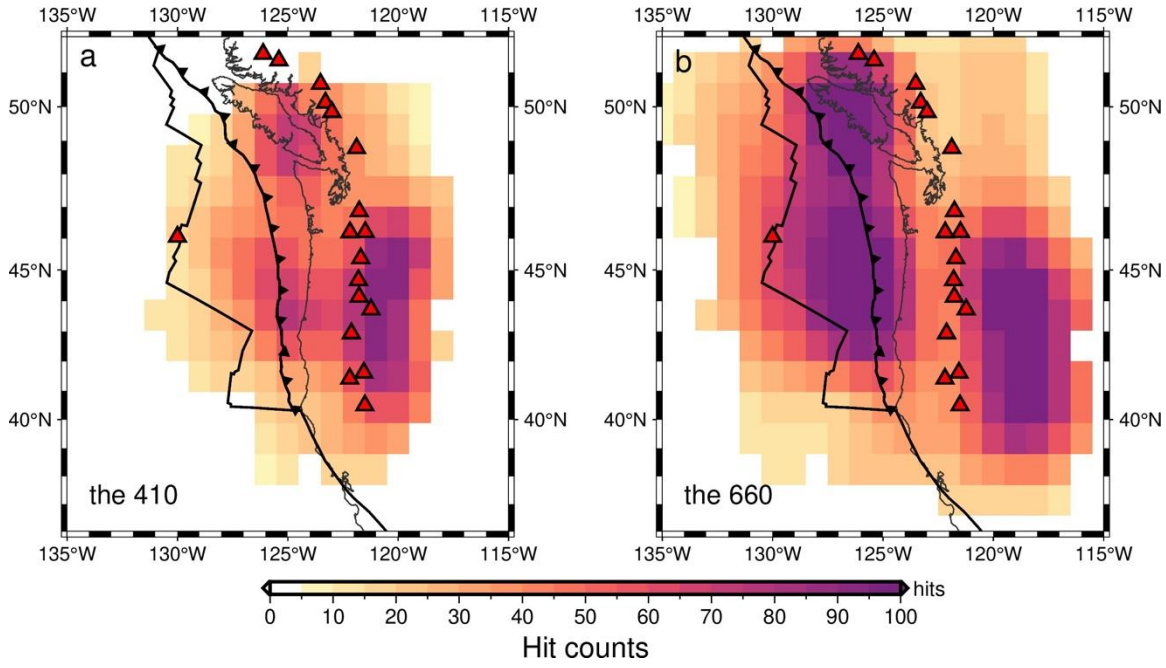

Figure S4. Hit counts maps at 410 and 660 km depths. Maps show numbers of waveforms stacked at 410 and 660 km.

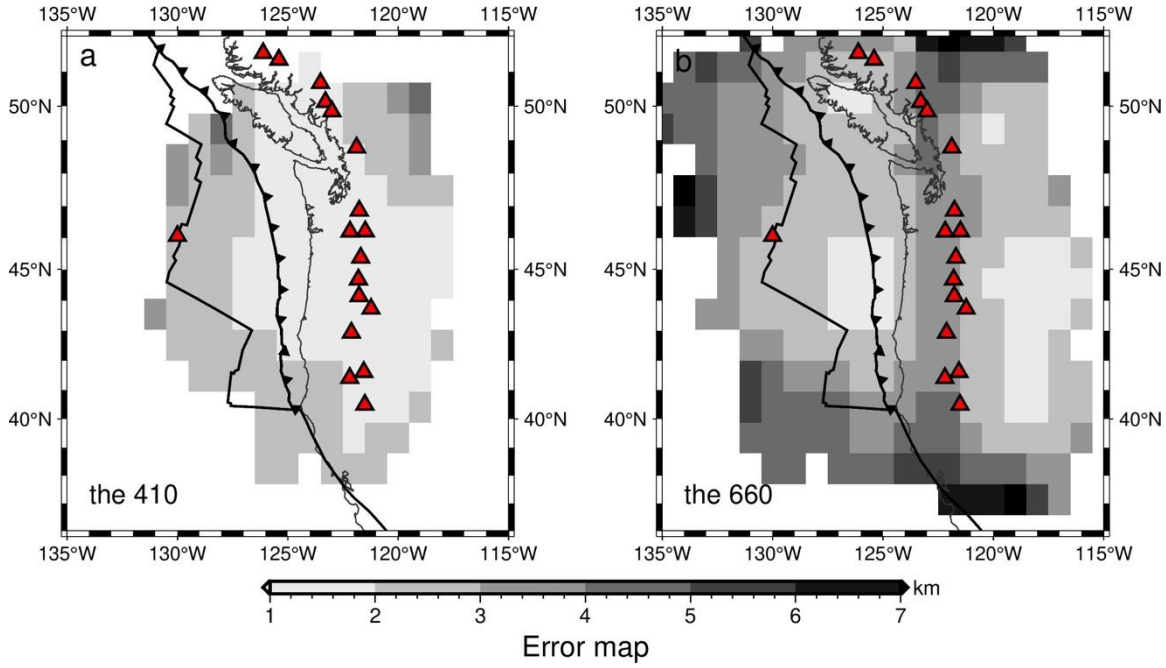

Figure S5. Error maps of the 410 and 660 depths. Maps show standard errors of means of the 410 and the 660 depths.

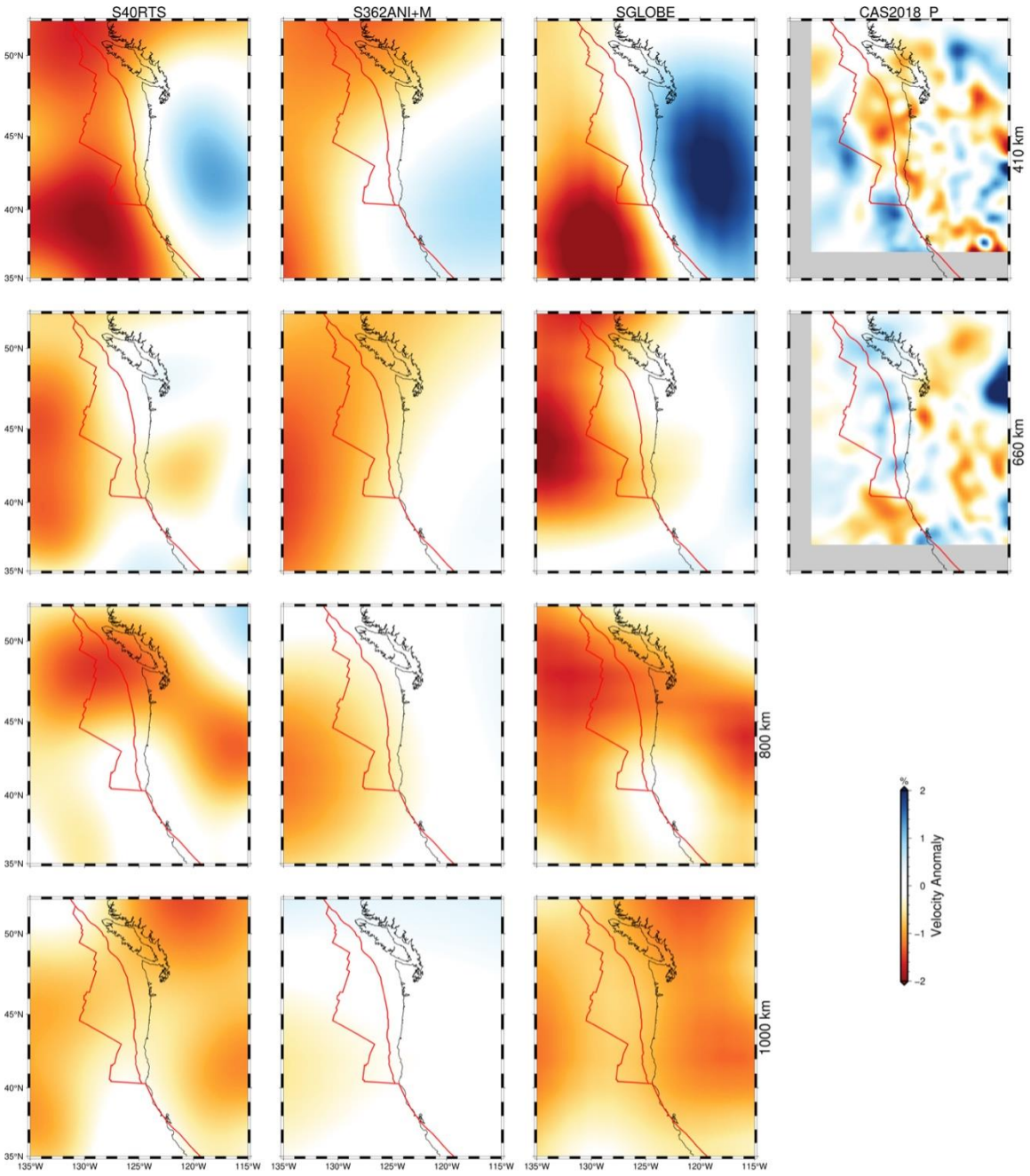

Figure S6. Horizontal slices of tomography models. Left 3 columns: Horizontal slices of global tomography models S40RTS (Ritsema et al., 2011), S362ANI+M (Moulik & Ekström, 2014), and SGLOBE (Chang et al., 2015) that share the same normal mode and overtone data combined with different types and combinations of surface wave and body wave data and tomography methods to resolve the mantle velocities at 410 km, 660 km, 800 km, and 1000 km. Right column: horizontal slices of regional P-wave velocity

anomalies model CAS2018_P (Bodmer et al., 2018) at 410 km and 660 km. The gray areas show the region outside the mode.

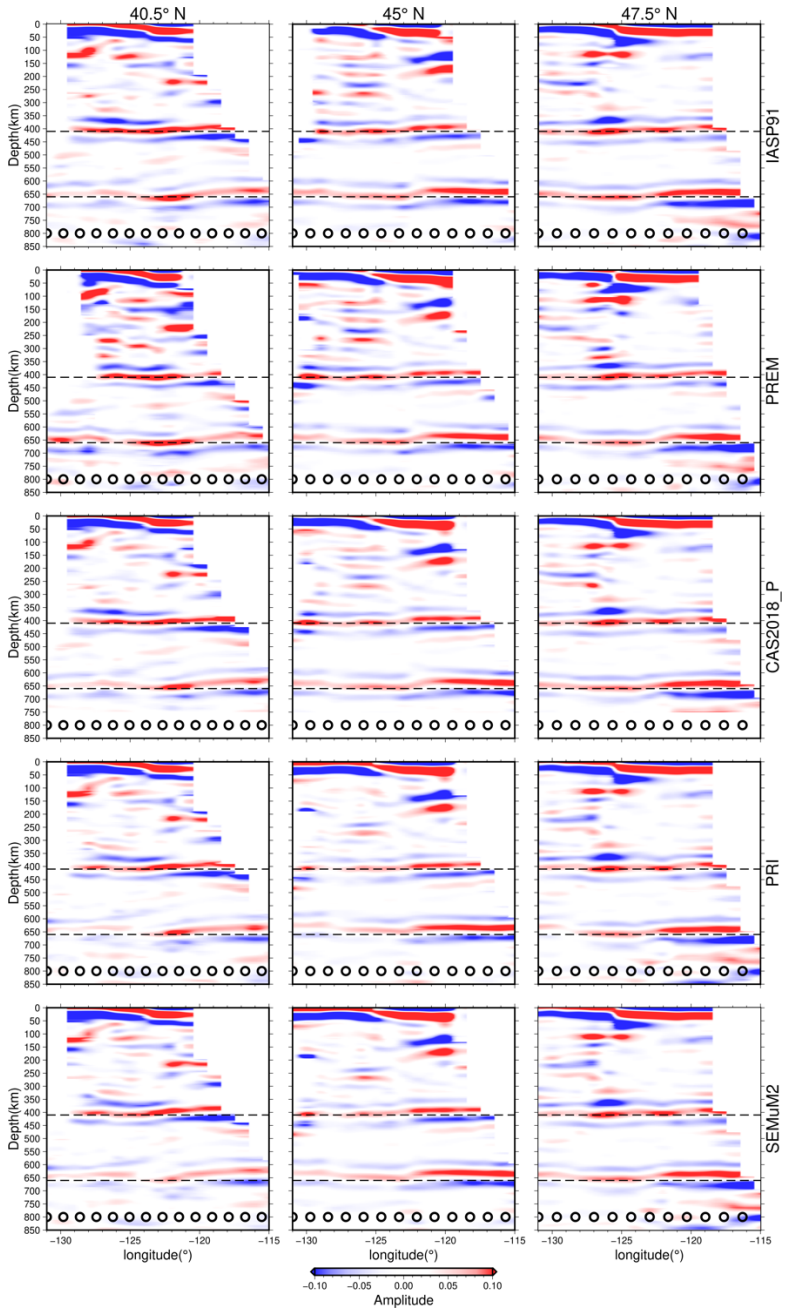

Figure S7. Migration tests (Vertical cross-sections). Vertical cross-sections similar to Figure 4 are shown for the following migration models: IASP91 (Kennett et al., 1995) (top), PREM (Dziewonski & Anderson, 1981) (second row), the 3-D dVp CAS2018_P (Bodmer et al., 2018) anomaly model related to absolute P-velocity assuming IASP91 for the reference model and calculating S-wave velocities assuming the Vp/Vs values from IASP91 (third row), 3-D Vs model SEMuM2 (French et al., 2013) with Vp/Vs ratio from IASP91 (bottom), and 3-D Vp and Vs models from PRI (Montelli et al., 2006) (fourth row).